Model Independent Approach of the JUNO ^{8}B Solar Neutrino Program

Jie Zhao[11], Baobiao Yue[21], Haoqi Lu[11], Yufeng Li *[11], Jiajie Ling †[21], Zeyuan Yu[11], Angel Abusleme[6,5], Thomas Adam[46], Shakeel Ahmad[67], Rizwan Ahmed[67], Sebastiano Aiello[56], Muhammad Akram[67], Abid Aleem[67], Tsagkarakis Alexandros[49], Fengpeng An[30], Qi An[23], Giuseppe Andronico[56], Nikolay Anfimov[68], Vito Antonelli[58], Tatiana Antoshkina[68], Burin Asavapibhop[72], João Pedro Athayde Marcondes de André[46], Didier Auguste[44], Weidong Bai[21], Nikita Balashov[68], Wander Baldini[57], Andrea Barresi[59], Davide Basilico[58], Eric Baussan[46], Marco Bellato[61], Antonio Bergnoli[61], Thilo Birkenfeld[49], Sylvie Blin[44], David Blum[55], Simon Blyth[11], Anastasia Bolshakova[68], Mathieu Bongrand[48], Clément Bordereau[45,41], Dominique Breton[44], Augusto Brigatti[58], Riccardo Brugnera[62], Riccardo Bruno[56], Antonio Budano[65], Jose Busto[47], Ilya Butorov[68], Anatael Cabrera[44], Barbara Caccianiga[58], Hao Cai[35], Xiao Cai[11], Yanke Cai[11], Zhiyan Cai[11], Riccardo Callegari[62], Antonio Cammi[60], Agustin Campeny[6], Chuanya Cao[11], Guofu Cao[11], Jun Cao[11], Rossella Caruso[56], Cédric Cerna[45], Chi Chan[39], Jinfan Chang[11], Yun Chang[40], Guoming Chen[29], Pingping Chen[19], Po-An Chen[41], Shaomin Chen[14], Xurong Chen[27], Yixue Chen[12], Yu Chen[21], Zhiyuan Chen[11], Zikang Chen[21], Jie Cheng[12], Yaping Cheng[8], Alexander Chepurnov[70], Alexey Chetverikov[68], Davide Chiesa[59], Pietro Chimenti[3], Artem Chukanov[68], Gérard Claverie[45], Catia Clementi[63], Barbara Clerbaux[2], Marta Colomer Molla[2], Selma Conforti Di Lorenzo[45], Daniele Corti[61], Flavio Dal Corso[61], Olivia Dalager[75], Christophe De La Taille[45], Zhi Deng[14], Ziyan Deng[11], Wilfried Depnering[52], Marco Diaz[6], Xuefeng Ding[58], Yayun Ding[11], Bayu Dirgantara[74], Sergey Dmitrievsky[68], Tadeas Dohnal[42], Dmitry Dolzhikov[68], Georgy Donchenko[70], Jianmeng Dong[14], Evgeny Doroshkevich[69], Marcos Dracos[46], Frédéric Druillole[45], Ran Du[11], Shuxian Du[38], Stefano Dusini[61], Martin Dvorak[42], Timo Enqvist[43], Heike Enzmann[52], Andrea Fabbri[65], Donghua Fan[25], Lei Fan[11], Jian Fang[11], Wenxing Fang[11], Marco Fargetta[56], Dmitry Fedoseev[68], Zhengyong Fei[11], Li-Cheng Feng[39], Qichun Feng[22], Richard Ford[58], Amélie Fournier[45], Haonan Gan[33], Feng Gao[49], Alberto Garfagnini[62], Arsenii Gavrikov[68], Marco Giammarchi[58], Nunzio Giudice[56], Maxim Gonchar[68], Guanghua Gong[14], Hui Gong[14], Yuri Gornushkin[68], Alexandre Göttel[51,49], Marco Grassi[62], Maxim Gromov[70], Vasily Gromov[68], Minghao Gu[11], Xiaofei Gu[38], Yu Gu[20], Mengyun Guan[11], Yuduo Guan[11], Nunzio Guardone[56], Cong Guo[11], Jingyuan Guo[21], Wanlei Guo[11], Xinheng Guo[9], Yuhang Guo[36], Paul Hackspacher[52], Caren Hagner[50], Ran Han[8], Yang Han[21], Miao He[11], Wei He[11], Tobias Heinz[55], Patrick Hellmuth[45], Yuekun Heng[11], Rafael Herrera[6], YuenKeung Hor[21], Shaojing Hou[11], Yee Hsiung[41], Bei-Zhen Hu[41], Hang Hu[21], Jianrun Hu[11], Jun Hu[11], Shouyang Hu[10], Tao Hu[11], Yuxiang Hu[11], Zhuojun Hu[21], Guihong Huang[25], Hanxiong Huang[10], Kaixuan Huang[21], Wenhao Huang[26], Xin Huang[11], Xingtao Huang[26], Yongbo Huang[29], Jiaqi Hui[31], Lei Huo[22], Wenju Huo[23], Cédric Huss[45], Safeer Hussain[67], Ara Ioannisian[1], Roberto Isocrate[61], Beatrice Jelmini[62], Ignacio Jeria[6], Xiaolu Ji[11], Huihui Jia[34], Junji Jia[35], Siyu Jian[10], Di Jiang[23], Wei Jiang[11], Xiaoshan Jiang[11], Xiaoping Jing[11], Cécile Jollet[45], Leonidas Kalousis[46], Philipp Kampmann[54,51], Li Kang[19],

Rebin Karaparambil[48], Narine Kazarian[1], Amina Khatun[71], Khanchai Khosonthongkee[74], Denis Korablev[68], Konstantin Kouzakov[70], Alexey Krasnoperov[68], Nikolay Kutovskiy[68], Pasi Kuusiniemi[43], Tobias Lachenmaier[55], Cecilia Landini[58], Sébastien Leblanc[45], Victor Lebrin[48], Frederic Lefevre[48], Ruiting Lei[19], Rupert Leitner[42], Jason Leung[39], Daozheng Li[11], Demin Li[38], Fei Li[11], Fule Li[14], Gaosong Li[11], Huiling Li[11], Mengzhao Li[11], Min Li[11], Nan Li[11], Nan Li[17], Qingjiang Li[17], Ruhui Li[11], Rui Li[31], Shanfeng Li[19], Tao Li[21], Teng Li[26], Weidong Li[11,15], Weiguo Li[11], Xiaomei Li[10], Xiaonan Li[11], Xinglong Li[10], Yi Li[19], Yichen Li[11], Zepeng Li[11], Zhaohan Li[11], Zhibing Li[21], Ziyuan Li[21], Zonghai Li[35], Hao Liang[10], Hao Liang[23], Jiajun Liao[21], Ayut Limphirat[74], Guey-Lin Lin[39], Shengxin Lin[19], Tao Lin[11], Ivano Lippi[61], Fang Liu[12], Haidong Liu[38], Haotian Liu[35], Hongbang Liu[29], Hongjuan Liu[24], Hongtao Liu[21], Hui Liu[20], Jianglai Liu[31,32], Jinchang Liu[11], Min Liu[24], Qian Liu[15], Qin Liu[23], Runxuan Liu[51,49], Shubin Liu[23], Shulin Liu[11], Xiaowei Liu[21], Xiwen Liu[29], Yan Liu[11], Yunzhe Liu[11], Alexey Lokhov[70,69], Paolo Lombardi[58], Claudio Lombardo[56], Kai Loo[52], Chuan Lu[33], Jingbin Lu[16], Junguang Lu[11], Shuxiang Lu[38], Bayarto Lubsandorzhiev[69], Sultim Lubsandorzhiev[69], Livia Ludhova[51,49], Arslan Lukanov[69], Daibin Luo[11], Fengjiao Luo[24], Guang Luo[21], Shu Luo[37], Wuming Luo[11], Xiaojie Luo[11], Vladimir Lyashuk[69], Bangzheng Ma[26], Bing Ma[38], Qiumei Ma[11], Si Ma[11], Xiaoyan Ma[11], Xubo Ma[12], Jihane Maalmi[44], Jingyu Mai[21], Yury Malyshkin[68], Roberto Carlos Mandujano[75], Fabio Mantovani[57], Francesco Manzali[62], Xin Mao[8], Yajun Mao[13], Stefano M. Mari[65], Filippo Marini[62], Cristina Martellini[65], Gisele Martin-Chassard[44], Agnese Martini[64], Matthias Mayer[53], Davit Mayilyan[1], Ints Mednieks[66], Yue Meng[31], Anselmo Meregaglia[45], Emanuela Meroni[58], David Meyhöfer[50], Mauro Mezzetto[61], Jonathan Miller[7], Lino Miramonti[58], Paolo Montini[65], Michele Montuschi[57], Axel Müller[55], Massimiliano Nastasi[59], Dmitry V. Naumov[68], Elena Naumova[68], Diana Navas-Nicolas[44], Igor Nemchenok[68], Minh Thuan Nguyen Thi[39], Alexey Nikolaev[70], Feipeng Ning[11], Zhe Ning[11], Hiroshi Nunokawa[4], Lothar Oberauer[53], Juan Pedro Ochoa-Ricoux[75,6,5], Alexander Olshevskiy[68], Domizia Orestano[65], Fausto Ortica[63], Rainer Othegraven[52], Alessandro Paoloni[64], Sergio Parmeggiano[58], Yatian Pei[11], Nicomede Pelliccia[63], Anguo Peng[24], Haiping Peng[23], Yu Peng[11], Zhaoyuan Peng[11], Frédéric Perrot[45], Pierre-Alexandre Petitjean[2], Fabrizio Petrucci[65], Oliver Pilarczyk[52], Luis Felipe Piñeres Rico[46], Artyom Popov[70], Pascal Poussot[46], Ezio Previtali[59], Fazhi Qi[11], Ming Qi[28], Sen Qian[11], Xiaohui Qian[11], Zhen Qian[21], Hao Qiao[13], Zhonghua Qin[11], Shoukang Qiu[24], Gioacchino Ranucci[58], Neill Raper[21], Alessandra Re[58], Henning Rebber[50], Abdel Rebii[45], Mariia Redchuk[62,61], Mariia Redchuk[62,61], Bin Ren[19], Jie Ren[10], Barbara Ricci[57], Mariam Rifai[51,49], Mathieu Roche[45], Narongkiat Rodphai[72], Aldo Romani[63], Bedřich Roskovec[42], Xichao Ruan[10], Arseniy Rybnikov[68], Andrey Sadovsky[68], Paolo Saggese[58], Simone Sanfilippo[65], Anut Sangka[73], Utane Sawangwit[73], Julia Sawatzki[53], Michaela Schever[51,49], Cédric Schwab[46], Konstantin Schweizer[53], Alexandr Selyunin[68], Andrea Serafini[62], Giulio Settanta[‡51], Mariangela Settimo[48], Zhuang Shao[36], Vladislav Sharov[68], Arina Shaydurova[68], Jingyan Shi[11], Yanan Shi[11], Vitaly Shutov[68], Andrey Sidorenkov[69], Fedor Šimkovic[71], Chiara Sirignano[62], Jaruchit Siripak[74], Monica Sisti[59], Maciej Slupecki[43], Mikhail Smirnov[21], Oleg Smirnov[68], Thiago Sogo-Bezerra[48], Sergey Sokolov[68], Julanan Songwadhana[74], Boonrucksar Soonthornthum[73], Albert Sotnikov[68], Ondřej Šrámek[42], Warintorn Sreethawong[74], Achim Stahl[49], Luca Stanco[61], Konstantin Stankevich[70], Dušan Štefánik[71], Hans Steiger[52,53], Jochen Steinmann[49], Tobias Sterr[55], Matthias Raphael Stock[53], Virginia Strati[57], Alexander Studenikin[70], Jun Su[21], Shifeng Sun[12], Xilei Sun[11], Yongjie

Sun[23], Yongzhao Sun[11], Zhengyang Sun[31], Narumon Suwonjandee[72], Michal Szelezniak[46], Jian Tang[21], Qiang Tang[21], Quan Tang[24], Xiao Tang[11], Alexander Tietzsch[55], Igor Tkachev[69], Tomas Tmej[42], Marco Danilo Claudio Torri[58], Konstantin Treskov[68], Andrea Triossi[62], Giancarlo Troni[6], Wladyslaw Trzaska[43], Cristina Tuve[56], Nikita Ushakov[69], Vadim Vedin[66], Giuseppe Verde[56], Maxim Vialkov[70], Benoit Viaud[48], Cornelius Moritz Vollbrecht[51,49], Cristina Volpe[44], Katharina von Sturm[62], Vit Vorobel[42], Dmitriy Voronin[69], Lucia Votano[64], Pablo Walker[6,5], Caishen Wang[19], Chung-Hsiang Wang[40], En Wang[38], Guoli Wang[22], Jian Wang[23], Jun Wang[21], Lu Wang[11], Meifen Wang[11], Meng Wang[24], Meng Wang[26], Ruiguang Wang[11], Siguang Wang[13], Wei Wang[28], Wei Wang[21], Wenshuai Wang[11], Xi Wang[17], Xiangyue Wang[21], Yangfu Wang[11], Yaoguang Wang[11], Yi Wang[14], Yi Wang[25], Yifang Wang[11], Yuanqing Wang[14], Yuman Wang[28], Zhe Wang[14], Zheng Wang[11], Zhimin Wang[11], Zongyi Wang[14], Apimook Watcharangkool[73], Wei Wei[11], Wei Wei[26], Wenlu Wei[11], Yadong Wei[19], Kaile Wen[11], Liangjian Wen[11], Christopher Wiebusch[49], Steven Chan-Fai Wong[21], Bjoern Wonsak[50], Diru Wu[11], Qun Wu[26], Zhi Wu[11], Michael Wurm[52], Jacques Wurtz[46], Christian Wysotzki[49], Yufei Xi[33], Dongmei Xia[18], Xiang Xiao[21], Xiaochuan Xie[29], Yuguang Xie[11], Zhangquan Xie[11], Zhao Xin[11], Zhizhong Xing[11], Benda Xu[14], Cheng Xu[24], Donglian Xu[32,31], Fanrong Xu[20], Hangkun Xu[11], Jilei Xu[11], Jing Xu[9], Meihang Xu[11], Yin Xu[34], Yu Xu[21], Baojun Yan[11], Taylor Yan[74], Wenqi Yan[11], Xiongbo Yan[11], Yupeng Yan[74], Changgen Yang[11], Chengfeng Yang[29], Huan Yang[11], Jie Yang[38], Lei Yang[19], Xiaoyu Yang[11], Yifan Yang[11], Yifan Yang[2], Haifeng Yao[11], Jiaxuan Ye[11], Mei Ye[11], Ziping Ye[32], Frédéric Yermia[48], Na Yin[26], Zhengyun You[21], Boxiang Yu[11], Chiye Yu[19], Chunxu Yu[34], Hongzhao Yu[21], Miao Yu[35], Xianghui Yu[34], Zezhong Yu[11], Cenxi Yuan[21], Chengzhuo Yuan[11], Ying Yuan[13], Zhenxiong Yuan[14], Noman Zafar[67], Vitalii Zavadskyi[68], Shan Zeng[11], Tingxuan Zeng[11], Yuda Zeng[21], Liang Zhan[11], Aiqiang Zhang[14], Bin Zhang[38], Binting Zhang[11], Feiyang Zhang[31], Guoqing Zhang[11], Honghao Zhang[21], Jialiang Zhang[28], Jiawen Zhang[11], Jie Zhang[11], Jin Zhang[29], Jingbo Zhang[22], Jinnan Zhang[11], Mohan Zhang[11], Peng Zhang[11], Qingmin Zhang[36], Shiqi Zhang[21], Shu Zhang[21], Tao Zhang[31], Xiaomei Zhang[11], Xin Zhang[11], Xuantong Zhang[11], Xueyao Zhang[26], Yinhong Zhang[11], Yiyu Zhang[11], Yongpeng Zhang[11], Yu Zhang[11], Yuanyuan Zhang[31], Yumei Zhang[21], Zhenyu Zhang[35], Zhijian Zhang[19], Fengyi Zhao[27], Rong Zhao[21], Runze Zhao[11], Shujun Zhao[38], Dongqin Zheng[20], Hua Zheng[19], Yangheng Zheng[15], Weirong Zhong[20], Jing Zhou[10], Li Zhou[11], Nan Zhou[23], Shun Zhou[11], Tong Zhou[11], Xiang Zhou[35], Jiang Zhu[21], Jingsen Zhu[30], Kangfu Zhu[36], Kejun Zhu[11], Zhihang Zhu[11], Bo Zhuang[11], Honglin Zhuang[11], Liang Zong[14], and Jiaheng Zou[11]

[1] *Yerevan Physics Institute, Yerevan, Armenia*
[2] *Université Libre de Bruxelles, Brussels, Belgium*
[3] *Universidade Estadual de Londrina, Londrina, Brazil*
[4] *Pontificia Universidade Catolica do Rio de Janeiro, Rio de Janeiro, Brazil*
[5] *Millennium Institute for SubAtomic Physics at the High-energy Frontier (SAPHIR), ANID, Chile*
[6] *Pontificia Universidad Católica de Chile, Santiago, Chile*
[7] *Universidad Tecnica Federico Santa Maria, Valparaiso, Chile*
[8] *Beijing Institute of Spacecraft Environment Engineering, Beijing, China*
[9] *Beijing Normal University, Beijing, China*
[10] *China Institute of Atomic Energy, Beijing, China*

[11] *Institute of High Energy Physics, Beijing, China*
[12] *North China Electric Power University, Beijing, China*
[13] *School of Physics, Peking University, Beijing, China*
[14] *Tsinghua University, Beijing, China*
[15] *University of Chinese Academy of Sciences, Beijing, China*
[16] *Jilin University, Changchun, China*
[17] *College of Electronic Science and Engineering, National University of Defense Technology, Changsha, China*
[18] *Chongqing University, Chongqing, China*
[19] *Dongguan University of Technology, Dongguan, China*
[20] *Jinan University, Guangzhou, China*
[21] *Sun Yat-Sen University, Guangzhou, China*
[22] *Harbin Institute of Technology, Harbin, China*
[23] *University of Science and Technology of China, Hefei, China*
[24] *The Radiochemistry and Nuclear Chemistry Group in University of South China, Hengyang, China*
[25] *Wuyi University, Jiangmen, China*
[26] *Shandong University, Jinan, China, and Key Laboratory of Particle Physics and Particle Irradiation of Ministry of Education, Shandong University, Qingdao, China*
[27] *Institute of Modern Physics, Chinese Academy of Sciences, Lanzhou, China*
[28] *Nanjing University, Nanjing, China*
[29] *Guangxi University, Nanning, China*
[30] *East China University of Science and Technology, Shanghai, China*
[31] *School of Physics and Astronomy, Shanghai Jiao Tong University, Shanghai, China*
[32] *Tsung-Dao Lee Institute, Shanghai Jiao Tong University, Shanghai, China*
[33] *Institute of Hydrogeology and Environmental Geology, Chinese Academy of Geological Sciences, Shijiazhuang, China*
[34] *Nankai University, Tianjin, China*
[35] *Wuhan University, Wuhan, China*
[36] *Xi'an Jiaotong University, Xi'an, China*
[37] *Xiamen University, Xiamen, China*
[38] *School of Physics and Microelectronics, Zhengzhou University, Zhengzhou, China*
[39] *Institute of Physics, National Yang Ming Chiao Tung University, Hsinchu*
[40] *National United University, Miao-Li*
[41] *Department of Physics, National Taiwan University, Taipei*
[42] *Charles University, Faculty of Mathematics and Physics, Prague, Czech Republic*
[43] *University of Jyvaskyla, Department of Physics, Jyvaskyla, Finland*
[44] *IJCLab, Université Paris-Saclay, CNRS/IN2P3, 91405 Orsay, France*
[45] *Univ. Bordeaux, CNRS, LP2i Bordeaux, UMR 5797, F-33170 Gradignan, France*
[46] *IPHC, Université de Strasbourg, CNRS/IN2P3, F-67037 Strasbourg, France*
[47] *Centre de Physique des Particules de Marseille, Marseille, France*
[48] *SUBATECH, Nantes Université, IMT Atlantique, CNRS-IN2P3, Nantes, France*
[49] *III. Physikalisches Institut B, RWTH Aachen University, Aachen, Germany*
[50] *Institute of Experimental Physics, University of Hamburg, Hamburg, Germany*
[51] *Forschungszentrum Jülich GmbH, Nuclear Physics Institute IKP-2, Jülich, Germany*

[52] *Institute of Physics and EC PRISMA$^+$, Johannes Gutenberg Universität Mainz, Mainz, Germany*
[53] *Technische Universität München, München, Germany*
[54] *Helmholtzzentrum für Schwerionenforschung, Planckstrasse 1, D-64291 Darmstadt, Germany*
[55] *Eberhard Karls Universität Tübingen, Physikalisches Institut, Tübingen, Germany*
[56] *INFN Catania and Dipartimento di Fisica e Astronomia dell Università di Catania, Catania, Italy*
[57] *Department of Physics and Earth Science, University of Ferrara and INFN Sezione di Ferrara, Ferrara, Italy*
[58] *INFN Sezione di Milano and Dipartimento di Fisica dell Università di Milano, Milano, Italy*
[59] *INFN Milano Bicocca and University of Milano Bicocca, Milano, Italy*
[60] *INFN Milano Bicocca and Politecnico of Milano, Milano, Italy*
[61] *INFN Sezione di Padova, Padova, Italy*
[62] *Dipartimento di Fisica e Astronomia dell'Università di Padova and INFN Sezione di Padova, Padova, Italy*
[63] *INFN Sezione di Perugia and Dipartimento di Chimica, Biologia e Biotecnologie dell'Università di Perugia, Perugia, Italy*
[64] *Laboratori Nazionali di Frascati dell'INFN, Roma, Italy*
[65] *University of Roma Tre and INFN Sezione Roma Tre, Roma, Italy*
[66] *Institute of Electronics and Computer Science, Riga, Latvia*
[67] *Pakistan Institute of Nuclear Science and Technology, Islamabad, Pakistan*
[68] *Joint Institute for Nuclear Research, Dubna, Russia*
[69] *Institute for Nuclear Research of the Russian Academy of Sciences, Moscow, Russia*
[70] *Lomonosov Moscow State University, Moscow, Russia*
[71] *Comenius University Bratislava, Faculty of Mathematics, Physics and Informatics, Bratislava, Slovakia*
[72] *Department of Physics, Faculty of Science, Chulalongkorn University, Bangkok, Thailand*
[73] *National Astronomical Research Institute of Thailand, Chiang Mai, Thailand*
[74] *Suranaree University of Technology, Nakhon Ratchasima, Thailand*
[75] *Department of Physics and Astronomy, University of California, Irvine, California, USA*

October 18, 2022

*E-mail: liyufeng@ihep.ac.cn (corresponding author)
†E-mail: lingjj5@mail.sysu.edu.cn (corresponding author)
‡Now at Istituto Superiore per la Protezione e la Ricerca Ambientale, Via Vitaliano Brancati, 48, 00144 Roma, Italy

Abstract

The physics potential of detecting ^{8}B solar neutrinos is exploited at the Jiangmen Underground Neutrino Observatory (JUNO), in a model independent manner by using three distinct channels of the charged-current (CC), neutral-current (NC) and elastic scattering (ES) interactions. Due to the largest-ever mass of ^{13}C nuclei in the liquid-scintillator detectors and the potential low background level, ^{8}B solar neutrinos would be observable in the CC and NC interactions on ^{13}C for the first time. By virtue of optimized event selections and muon veto strategies, backgrounds from the accidental coincidence, muon-induced isotopes, and external backgrounds can be greatly suppressed. Excellent signal-to-background ratios can be achieved in the CC, NC and ES channels to guarantee the ^{8}B solar neutrino observation. From the sensitivity studies performed in this work, we show that one can reach the precision levels of 5%, 8% and 20% for the ^{8}B neutrino flux, $\sin^2\theta_{12}$, and Δm^2_{21}, respectively, using ten years of JUNO data. It would be unique and helpful to probe the details of both solar physics and neutrino physics. In addition, when combined with SNO, the world-best precision of 3% is expected for the ^{8}B neutrino flux measurement.

1 Introduction

Electron neutrino fluxes are produced from thermal nuclear fusion reactions in the solar core, either through the proton-proton (*pp*) chain or the Carbon-Nitrogen-Oxygen (CNO) cycle. According to their production reactions, the solar neutrino species can be categorized as *pp*, ^{7}Be, *pep*, ^{8}B, *hep* neutrinos of the *pp* chain, and ^{13}N, ^{15}O, and ^{17}F neutrinos of the CNO cycle. Before reaching the detector, solar neutrinos undergo the flavor conversion inside the Sun and the Earth during their propagation. It has been a long history for solar neutrino physics since the first observation at the Homestake experiment [1]. Many measurements, such as Kamiokande [2], GALLEX/GNO [3, 4], SAGE [5], and Super-Kamiokande (SK) [6, 7], had observed the solar neutrino deficit problem: that is the amount of observed neutrinos originating from the Sun was much less than that expected from the Standard Solar Model (SSM). Subsequently, the Sudbury Neutrino Observatory (SNO) provided the first model-independent evidence of the solar neutrino flavor conversion using three distinct neutrino interaction channels in heavy water [8–14]. These reactions include the ν_e sensitive charged-current (CC) interaction, all flavor sensitive neutral-current (NC) interaction on Deuterium, and the elastic scattering (ES) interaction on electrons from all neutrino flavors with different cross sections.

Solar neutrino observations rely on both the flux prediction from the SSM and neutrino oscillation parameters that determine the flavor conversion [15–17]. Thus although SK [18,19] and Borexino [20, 21] experiments have made precision measurements on the ^{8}B neutrinos via the ES interaction, the evaluation of the total amount of neutrinos produced inside the Sun relies on the input of solar neutrino oscillations [17]. The present most precise ^{8}B neutrino flux is determined by SNO with the precision of 3.8% [10–14], and it is the only existing model independent flux measurement. Therefore, a second independent measurement of the total ^{8}B neutrino flux with the NC channel [22, 23] would be important to answer relevant questions in the field of solar physics. For example, there is the solar abundance problem, in which the SSM based on the solar composition with a higher value of metallicity is inconsistent with the helioseismological measurements [24].

In contrast, the neutrino oscillation parameters $\sin^2\theta_{12}$ and Δm^2_{21} have reached the precision levels around 5% and 15% respectively, from the current global solar neutrino data [25]. The mixing angle $\sin^2\theta_{12}$ is extracted from the comparison of the observed fluxes of *pp*, ^{7}Be, and ^{8}B solar neutrinos to their respective total fluxes from the SSM. And the mass squared difference Δm^2_{21} is measured from both the vacuum-matter transition of the ^{8}B neutrino oscillations and the size of the day-night asymmetry. A direct comparison of oscillation parameters from the solar neutrino and reactor antineutrino oscillations is an unique probe of new physics beyond the Standard Model of particle physics. It would be excellent to have a new measurement of solar neutrino oscillations with high precision in this respect. This has triggered a variety of interesting discussions on the prospects of future large neutrino detectors [26–29].

The Jianmen Underground Neutrino Observatory (JUNO) is a liquid scintillator (LS) detector of 20 kton, which is located in South China and will start data taking by 2023. As a multiple-purpose neutrino experiment, JUNO is unique for the solar neutrino detection because of its large target mass, excellent energy resolution, and expected low background levels. With the analysis threshold cut of around 2 MeV for the recoiled electron energies in the ES channel, JUNO can make a high-statistics measurement of the flux and spectral shape of ^{8}B solar neutrinos and will be able to extract the neutrino oscillation parameters $\sin^2\theta_{12}$ and Δm^2_{21} [27]. In addition to the high statistics measurement in the ES channel, the presence of a large mass of the ^{13}C nuclei ($\sim$0.2 kt) makes it feasible to detect ^{8}B solar neutrinos via CC and NC interactions on ^{13}C. By combining all the CC,

Table 1: Typical CC, NC, and ES detection channels of the ^{8}B solar neutrinos together with the final states, the neutrino energy threshold, the typical signatures in the detector, and the expected event numbers with 10 years of data taking. Note that ν_x with $(x = e, \mu, \tau)$ denotes all three active flavor neutrinos. The spin and parity of the daughter nuclei at the ground (gnd) or excited states, denoted as the corresponding excited energies, are also provided.

No.	Channels		Threshold [MeV]	Signal	Event numbers (10 years)
1	CC	$\nu_e + ^{12}\mathrm{C} \to e^- + ^{12}\mathrm{N}\,(1^+;\mathrm{gnd})$ [32]	16.827	e^-+^{12}N decay (β^+, Q=17.338 MeV)	0.43
1		$\nu_e + ^{13}\mathrm{C} \to e^- + ^{13}\mathrm{N}\,(\frac{1}{2}^-;\mathrm{gnd})$ [33]	2.2	e^-+^{13}N decay (β^+, Q=2.22 MeV)	3929
2		$\nu_e + ^{13}\mathrm{C} \to e^- + ^{13}\mathrm{N}\,(\frac{3}{2}^-;3.5\,\mathrm{MeV})$ [33]	5.7	e^-+p	2464
4	NC	$\nu_x + ^{12}\mathrm{C} \to \nu_x + ^{12}\mathrm{C}\,(1^+;15.11\,\mathrm{MeV})$ [32]	15.1	γ	4.8
3		$\nu_x + ^{13}\mathrm{C} \to \nu_x + n + ^{12}\mathrm{C}\,(2^+;4.44\,\mathrm{MeV})$ [34]	6.864	$\gamma + n$ capture	65
4		$\nu_x + ^{13}\mathrm{C} \to \nu_x + ^{13}\mathrm{C}\,(\frac{1}{2}^+;3.089\,\mathrm{MeV})$ [33]	3.089	γ	14
5		$\nu_x + ^{13}\mathrm{C} \to \nu_x + ^{13}\mathrm{C}\,(\frac{3}{2}^-;3.685\,\mathrm{MeV})$ [33]	3.685	γ	3032
6		$\nu_x + ^{13}\mathrm{C} \to \nu_x + ^{13}\mathrm{C}\,(\frac{5}{2}^+;3.854\,\mathrm{MeV})$ [33]	3.854	γ	2.8
7	ES	$\nu_x + e \to \nu_x + e$	0	e^-	3.0×10^5

NC and ES channels, we are able to perform a model independent measurement of the ^{8}B solar neutrino flux and oscillation parameters $\sin^2\theta_{12}$ and Δm^2_{21}, which will add a unique contribution to the global solar neutrino program.

The paper is organized as follows. We illustrate the typical signatures of the CC and NC interactions of ^{8}B solar neutrinos, and evaluate the corresponding backgrounds in the JUNO detector in Sec. 2. In Sec. 3, the physics potential of detecting the ^{8}B solar neutrinos with different combinations of the CC, NC, and ES channels are presented, and the sensitivity to the ^{8}B solar neutrino flux, $\sin^2\theta_{12}$ and Δm^2_{21} is reported. The concluding remarks of this study are presented in Sec. 4.

2 Signal and Background at JUNO

The JUNO experiment is building the world largest LS detector with the total target mass of 20 kt, in which the mass fraction of Carbon is 88%. Given that the natural abundance of ^{13}C is 1.1%, the mass of ^{13}C can reach the level of $\sim$0.2 kt, which is similar to the total mass of Deuterium of the SNO detector. Therefore, the CC and NC solar neutrino interaction rates on the ^{13}C nuclei will be sizable at JUNO.

In Table 1, we present the typical CC, NC and ES detection channels for ^{8}B solar neutrinos in the LS medium. For each interaction channel, the reaction threshold is provided, together with the typical experimental signatures, and the expected event numbers for 10 years of data taking before event selection cuts. The spin and parity of the daughter nuclei at the ground (gnd) or excited state, denoted by the corresponding excited energies, are also provided. The unoscillated ^{8}B solar neutrino ν_e flux (5.25×10^6 /cm^2/s) is taken from the final result of SNO for this estimation [14], and the spectra are taken from Refs. [30, 31]. The cross sections for these exclusive channels are taken from the calculation in Refs. [32–34], in which the uncertainties at the level of a few percent are considered to be achievable. Note that the standard Mikheev-Smirnov-Wolfenstein (MSW) effect of solar neutrino oscillations [15, 16] and the neutrino oscillation parameters from Ref. [17] are used in the signal calculations of the CC, NC, and ES channels.

There are no interactions on the ^{12}C nuclei for most solar neutrinos because of the high energy threshold. Thus for the CC channel, we are left with the following exclusive interaction:

$$\nu_e + ^{13}\mathrm{C} \to e^- + ^{13}\mathrm{N}\left(\frac{1}{2}^-;\mathrm{gnd}\right), \tag{1}$$

where the final ^{13}N is in the ground state. It undergoes a delayed β^+ decay ($Q = 2.2$ MeV) with a lifetime of 863 s. The distinct signature for this channel is a coincidence of the prompt electron and delayed positron with stringent time, distance, and energy requirements. The expected number of events for ^{8}B solar neutrinos in this CC channel is 3929 for 10 years of data taking. Note that the CC interaction channel with an excited $^{13}\mathrm{N}\,(3/2^-; 3.502\,\mathrm{MeV})$ in the final state has a comparable cross section as the ground-state channel [33], but the deexcitation of $^{13}\mathrm{N}\,(3/2^-; 3.502\,\mathrm{MeV})$ is dominated by a proton knockout. The corresponding signature after quenching is a single event and thus cannot be distinguished from the recoiled electron of the ES channel on an event-by-event basis.

Among all the five listed NC channels, the only one with a coincidence signature is the interaction of $\nu_x + ^{13}\mathrm{C} \to \nu_x + n + ^{12}\mathrm{C}$, with a prompt γ energy of 4.44 MeV from ^{12}C de-excitation and the delayed neutron capture. However, given that the background from the inverse beta decay interactions of reactor antineutrinos are overwhelming, where the signal to background ratio is at the level of 10^{-4}, and thus the event rate of this channel is unobservable. In this work we focus on the NC channels with the signature of single γ deexcitation, among which the NC interaction with the ^{13}C de-excited energy of 3.685 MeV:

$$\nu_x + ^{13}\mathrm{C} \to \nu_x + ^{13}\mathrm{C}\left(\frac{3}{2}^-; 3.685\,\mathrm{MeV}\right) , \tag{2}$$

is the dominant interaction channel and will be used to determine the ^{8}B solar neutrino flux via the NC interaction.

Finally, we also consider the ES interaction channel on the electron,

$$\nu_x + e \to \nu_x + e , \tag{3}$$

where the signature is a single recoiled electron [27]. Using all the three channels of CC, NC, ES interactions, we are able to make a model independent measurement of the ^{8}B solar neutrino flux, $\sin^2\theta_{12}$ and Δm^2_{21} with JUNO, which is useful to disentangle the solar dynamics and the neutrino oscillation effects. This measurement is expected to be the only model independent study after the SNO experiment [9–12].

To summarize, in this work we are going to employ the following three interaction channels for a model independent approach of the JUNO ^{8}B solar neutrino program: i) the CC detection channel is sensitive to the ν_e component of solar neutrinos, ii) the NC channel is sensitive to all active neutrino flavors (ν_e, ν_μ, ν_τ) with identical cross sections, iii) the ES channel is also sensitive to all active flavors, but with a preferred cross section for the ν_e flux [i.e., $\sigma(\nu_{\mu/\tau}) \simeq 0.17\,\sigma(\nu_e)$].

2.1 $\nu_e + ^{13}\mathrm{C}$ Charged Current Channel

For the typical coincidence signature of the CC channel, $\nu_e + ^{13}\mathrm{C} \to e^- + ^{13}\mathrm{N}\,(1/2^-; \mathrm{gnd})$, the energy of the prompt signal is the kinetic energy of the outgoing electron with the reaction threshold of 2.2 MeV. Therefore, there is a one-to-one correspondence between the electron kinetic energy and the initial neutrino energy $T_e \simeq E_\nu - 2.2$ MeV, because of the negligible recoil energy of the daughter ^{13}N. Meanwhile, the delayed signal is the deposited energy of the positron from the ^{13}N β^+ decay ($Q = 2.2$ MeV), with a decay lifetime of $\tau = 863$ s. The time and spatial correlation between the prompt and delayed signals provides the distinct feature of the coincidence signature.

In the following, we consider two significant backgrounds for this coincidence signature of the CC channel in this work.

- The first background is the accidental coincidence of two single events. For the visible energy between 2 and 5 MeV, natural radioactivity composes the most significant part of the prompt

Table 2: The efficiencies of optimized event selection cuts for the signal and backgrounds of the ν_e CC channel [$\nu_e + ^{13}\mathrm{C} \rightarrow e^- + ^{13}\mathrm{N}\,(1/2^-;\mathrm{gnd})$] analysis. The expected event numbers of the signal and backgrounds for 10 years of data taking after each cut are also listed. The fiducial volume used in this work corresponds to the effective mass of 16.2 kt. For the energy cuts, E_p and E_d represent the visible energy of prompt and delayed signals. The same muon and three-fold-coincidence veto strategies as in Ref. [27] are used for the reduction of muon-induced isotopes.

	Cuts	CC signal efficiency	CC signal	Background for CC channel		
				Solar ES	Muon-induced isotopes	
				Accidental	Accidental	Correlated
–	–	–	3929	–	–	–
Time cut	$\Delta T < 900$ s	65%	2554	10^{10}	10^{13}	10^{12}
Energy cut	5 MeV $< E_p <$14 MeV 1 MeV $< E_d <$ 2 MeV	79% 91%	1836	10^9	10^{10}	10^9
Fiducial volume Cut	$R < 16.5$ m [27]	81%	1487	10^7	10^7	10^8
Vertex cut	$\Delta d < 0.47$ m	87%	1293	328	10^5	10^6
Muon veto	Muon and TFC veto [27]	50%	647	164	53	58
Combined	–	17%	647	275		

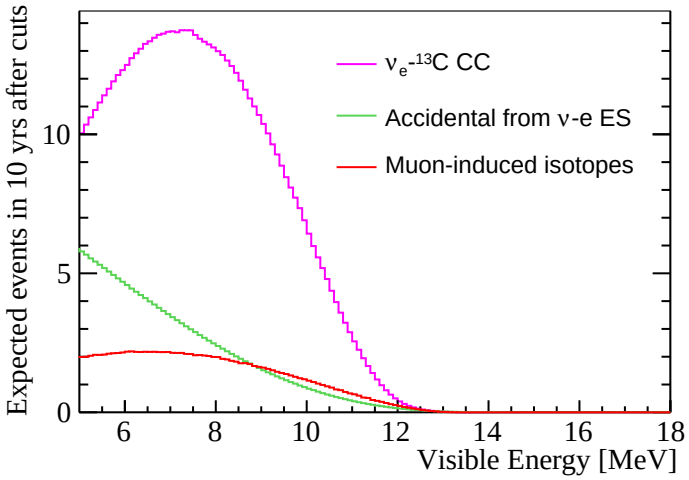

Figure 1: Expected prompt visible energy spectra of the CC signal and backgrounds after the optimized cuts. The accidental background with the recoiled electron from solar neutrino ES interaction as the prompt signal is illustrated as the green line. The background from muon-induced isotopes is illustrated as the red line, which is the summation of the accidental and correlated backgrounds originated from the initial muons.

component of the coincidence candidate, while the prompt signals above 5 MeV come from the muon-induced unstable isotopes and the recoiled electrons of solar neutrino ES interactions. Due to the expected natural radioactivity level in the LS (10^{-17} g/g ^{238}U and ^{232}Th in the secular equilibrium, 10^{-18} g/g ^{40}K and 10^{-24} g/g ^{210}Pb), a requirement on the selection of the prompt energy is to minimize the contribution from these radioactivity events. The delayed component of the accidental background is mainly from the cosmogenic ^{11}C decay ($Q = 1.98$ MeV) in the energy range of [1, 2] MeV, while the internal LS radioactivity contributes less than 2% compared to that from ^{11}C. If the internal radioactivity is 1-2 orders of magnitude higher than expected, the contribution to the delayed component from the radioactivity would be at the same level as the cosmogenic ^{11}C decay. Note that all the single events in the energy range between 1 and 2 MeV can be accurately measured in-situ with the future data, and the accidental background can be deduced with the off-time coincidence method. Note that we have neglected the external radioactivity which can be effectively removed by the proper fiducial volume cut.

- The second background is produced by the correlated prompt and delayed decays of unstable isotopes from the same parent muon. These correlated decays are not considered in the above accidental background. Therefore, the cosmic muon and the corresponding isotope simulations have been performed, and the muon veto strategies of the three-fold-coincidence are the same as those in Ref. [27]. It shows that the prompt signal is mainly from the beta decays of ^{12}B, ^{8}Li, ^{6}He, and ^{10}C (below 4 MeV), and as expected the delayed signal is from ^{11}C. The muon detection efficiency of the outer water veto can reach as high as 99.5% [27]. Since the remaining untagged muons are usually located at the edge of the central detector, these muon-induced correlated background can be removed using the fiducial volume cut and is neglected in this work. Note that we have assumed a perfect detector uniformity for these isotopes and used the whole detector region to estimate the background inside the fiducial volume.

We have simulated the signal and backgrounds using the official JUNO simulation software [35, 36]. According to the signal characteristics of the CC channel, the accidental background can be calculated with different selection cuts. The final event selection criteria is obtained by optimizing the figure of merit, $S/\sqrt{S+B}$, where S and B stand for the rates of the signal and background, respectively. The optimized event selection cuts of the fiducial volume, the prompt and delayed energies, the time and spatial correlation cuts and muon vetos are provided step by step in Tab. 2, where the efficiencies of the signal and backgrounds are also calculated. In order to avoid possible large contamination from the internal radioactivity and muon-induced ^{10}C, we select the threshold of the prompt visible energy to 5 MeV for the CC channel, i.e., 5 MeV $< E_p <$ 14 MeV. Meanwhile, the fiducial volume is chosen to be $R < 16.5$ m to reject the external radioactivity and isotopes, with R being the distance to the detector center.

We illustrate in Fig. 1 the expected prompt visible energy spectra of the selected signal and residual backgrounds in the CC channel after the optimized cuts. The expected number of selected signals is 647 for 10 years of data taking, which is shown as the purple line. The fiducial volume used in this work corresponds to the effective mass of 16.2 kt. The accidental background with solar neutrino ES interactions as the prompt signal is illustrated as the green line and contributes 164 background events, which will be fully correlated with the solar neutrino ES signal in the following global analysis. In contrast, the muon-induced isotopes contribute 111 background events (depicted as the red line of Fig. 1), which are from both the accidental coincidence (53 events) and correlated background (58 events). Therefore, we can achieve an excellent $S/\sqrt{S+B} \simeq 21$.

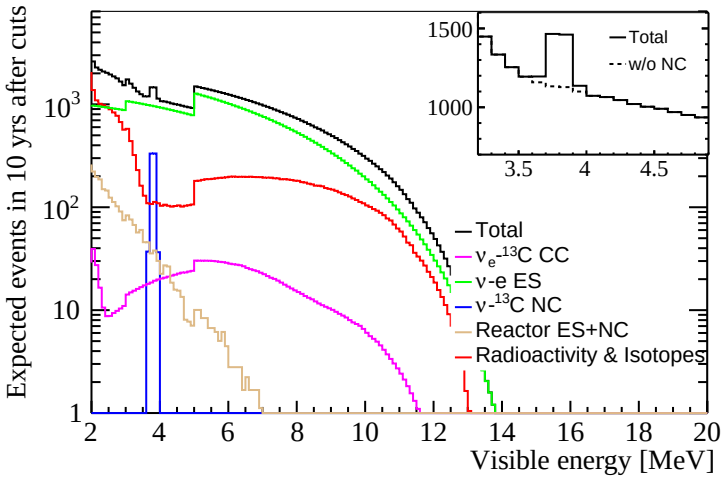

Figure 2: Expected visible energy spectra of all single event sources for 10 years of data taking with the same energy-dependent fiducial volume cuts as in Ref. [27] are illustrated. The blue and green curves are singles from the ν_x+^{13}C NC and ν_x+e ES channels, respectively. The purple curve includes the $\nu_e + {}^{13}\mathrm{C} \to e^- + {}^{13}\mathrm{N}\,(\frac{3}{2}^-)$ channel and the residual singles of the $\nu_e + {}^{13}\mathrm{C} \to e^- + {}^{13}\mathrm{N}\,(\frac{1}{2}^-)$ channel after the coincidence cut. The red curve represents the single events from natural radioactivity and muon-induced unstable isotopes. The brown curve includes the $\bar{\nu}_e + e$ ES and $\bar{\nu}_x + {}^{13}\mathrm{C}$ NC channels from reactor antineutrinos. The black curve is the summation of all the components. The upper right insert plot is illustrated for the energy range between 3 and 5 MeV in the linear scale. Note that the discontinuities at 3 MeV and 5 MeV are due to the changes in the fiducial volume size.

Finally, the expected event number of *hep* solar neutrinos in the CC channel is about 15 for ten years of data taking, but only 3 events are beyond the spectral tail of ^{8}B solar neutrinos. Thus it would be difficult to detect the *hep* solar neutrinos with the CC interaction on ^{13}C, and the signal from the *hep* solar neutrinos will be neglected in this work.

2.2 $\nu_x + {}^{13}\mathrm{C}$ Neutral Current Channel

The typical signature for the NC event, $\nu_x + {}^{13}\mathrm{C} \to \nu_x + {}^{13}\mathrm{C}\,(3/2^-; 3.685\,\mathrm{MeV})$ is a mono-energetic γ with the energy of 3.685 MeV, convoluted with the detector energy resolution of $3\%/\sqrt{E}$. The expected visible energy spectra of all single event sources for 10 years of data taking with the same energy-dependent fiducial volume cuts as in Ref. [27] are shown in Fig. 2. The blue and green curves are singles from the $\nu_x + {}^{13}\mathrm{C}$ NC and $\nu_x + e$ ES channels, respectively. The purple curve includes the $\nu_e + {}^{13}\mathrm{C} \to e^- + {}^{13}\mathrm{N}\,(\frac{3}{2}^-)$ channel and the residual singles of the $\nu_e + {}^{13}\mathrm{C} \to e^- + {}^{13}\mathrm{N}\,(\frac{1}{2}^-)$ channel after the coincidence cut. The red curve represents the single events from natural radioactivity and muon-induced unstable isotopes [27]. The brown curve includes the $\bar{\nu}_e + e$ ES and $\bar{\nu}_x + {}^{13}\mathrm{C}$ NC channels from reactor antineutrinos. The NC events rate from reactor antineutrinos is less than 0.2% of that from solar neutrinos. The black curve is the summation of all the components. Note that the discontinuities at 3 MeV and 5 MeV are caused by the energy-dependent fiducial volume cuts which are, from low to high energies, $R < 13$ m for [2, 3] MeV, $R < 15$ m for [3, 5] MeV, and $R < 16.5$ m for the energies large than 5 MeV. The upper right insert plot is illustrated for the energy range between 3 to 5 MeV in the linear scale, where a clear peak from the solar neutrino NC channel can be seen above the continuous spectra from solar neutrino ES interactions and the other backgrounds, demonstrating the promising prospect for the observation of the NC channel at

JUNO. After all the cuts the number of signal events in the NC channel is 738 for 10 years of data taking.

2.3 $\nu_x + e$ Elastic Scattering Channel

In this work, we follow exactly the same strategy as in Ref. [27] for the analysis of the $\nu_x + e$ ES channel, where energy spectra for the recoiled electrons as well as all the backgrounds have been shown in Fig. 2. One should note that the upturn feature of the energy dependence of the solar neutrino survival probability is clearly visible in the electron energy spectrum.

2.4 Day-Night Asymmetry

The MSW effect can cause solar neutrino event rate variations as a function of the solar zenith angle when the neutrinos propagate through the Earth [37–45], and result in the day-night asymmetry of the solar neutrino observation, in which the signal rate in the night is higher than that in the day due to ν_e regeneration inside the Earth.

In this work, in addition to the visible energy spectra of the CC, NC and ES channels, we also consider the day-night asymmetry to constrain the neutrino oscillation parameters. The location of JUNO (i.e., 112°31'05" E and 22°07'05" N [46]) is used in the day-night asymmetry calculations, and the two dimensional visible energy and zenith angle spectra are employed. For illustration, we show in Fig. 3 the ratios of solar neutrino signal event rates with and without considering the terrestrial matter effects as the function of the zenith angle θ_z. The red and blue solid lines are for the ES and CC channels, respectively. In comparison, the dashed lines are shown for the respective averages over the whole zenith angle range. The ratios of the day-night average ($R_{\rm A}$), the daytime ($R_{\rm D}$), and the nighttime ($R_{\rm N}$) are also illustrated with the first three bins. The error bars are quoted as the statistical uncertainties of the signal and backgrounds. The blue shaded regions with different colors from the left to right are used to denote the zenith angle ranges passing through the crust, mantle and core of the Earth respectively. The day-night asymmetry, defined as $(R_{\rm D} - R_{\rm N})/R_{\rm A}$, is predicted to be -3.1% and -1.6% for the CC and ES channels respectively. The energy ranges of the CC and ES channels are [5, 14] MeV and [2, 16] MeV respectively. Given that all the neutrino flavors can be detected through the NC channel, no day-night asymmetry exists in the NC detection. Note that the magnitude of the day-night asymmetry strongly depends on the value of Δm^2_{21}. If Δm^2_{21} is decreased from the KamLAND measurement 7.5×10^{-5} eV^2 [17] to 6.1×10^{-5} eV^2 of the global solar neutrino data [25], the absolute values of the day-night asymmetry are also increased to -4.2% and -2.2% for the CC and ES channels, respectively.

3 Sensitivity Study

In this section, we study the physical potential for the model independent measurement of ^{8}B solar neutrinos using CC, NC, and ES channels. Based on the typical event signatures, the full solar neutrino data can be separated into the correlated and single event data sets. As discussed in the previous section, all the three interaction channels from ^{8}B solar neutrinos would contribute to the single event data set, while the correlated data set includes events from both the CC channel and the accidental coincidence of the ES channel.

In this analysis, we consider the following systematic uncertainties. First, the uncertainty of detection efficiency is estimated to be 2% [27], which is fully correlated for the the signal and background components of each data set, but uncorrelated between the coincidence and single event

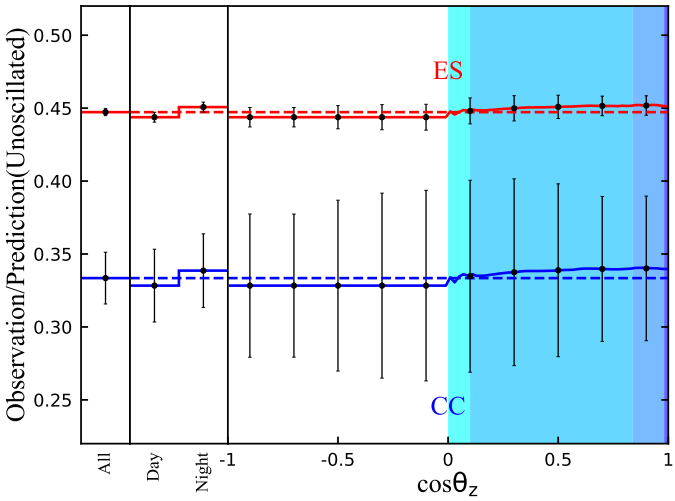

Figure 3: Ratios of the solar neutrino signal event rates with and without considering terrestrial matter effects as the function of the zenith angle for the ES (red sold line) and CC (blue solid line) channels. The dashed lines are shown for the average over the whole zenith angle range. The ratios for the daytime, nighttime and the day-night average are also shown for comparison. The blue shaded regions with different colors from the left to right are used to denote the zenith angle ranges passing through the crust, mantle and core of the Earth. Note that the signal rate in the night is higher than that in the day due to the ν_e regeneration through the Earth.

data samples. Second, the current uncertainty of the ^{13}C cross sections from the model calculation is at the level of several percents [32–34], but the precision could be reduced to 1% or better with large-scale modern shell-model calculations [47]. Therefore the uncertainties for the ^{13}C CC and NC interaction are taken as 1% for the current study. A 0.5% cross section uncertainty is used for the ES channel [48]. Third, the shape uncertainty of ^{8}B solar neutrinos is taken from Refs. [30, 31], and the uncertainties for the radioactive and muon-induced backgrounds are the same as those in Ref. [27], namely, 1% for ^{238}U, ^{232}Th and ^{12}B decays, 3% for ^{8}Li and ^{6}He decays, and 10% for ^{10}C and ^{11}Be decays. A 2% uncertainty is used for the single event from the reactor antineutrino ES interaction. In this work we treat the ^{8}B solar neutrino flux as a free parameter since we are performing the model independent measurement. Only in the scenario of combining with the SNO flux measurement, an uncertainty of 3.8% is used as an informative prior.

The standard Poisson-type χ^2 method using the Asimov data set [17] is employed to estimate the sensitivity to measure the ^{8}B solar neutrino flux and the oscillation parameters $\sin^2\theta_{12}$ and Δm^2_{21}, where different pull parameters are included in the χ^2 function to account for the systematic uncertainties described in this section. More technical details on the construction of the χ^2 function are provided in the Appendix. In order to identify the contribution of each interaction channel, we divide the whole data sets into the correlated events, the single events within [3.5, 4.1] MeV, and the single events outside [3.5, 4.1] MeV, which correspond to the CC, NC, and ES measurements respectively.

We illustrate in Figs 4-6 the two dimensional allowed ranges and the marginalized one dimensional curves on the sensitivity of the ^{8}B neutrino flux, $\sin^2\theta_{12}$ and Δm^2_{21}, of which Fig. 4 is for the comparison of the ES and ES+NC measurements, Fig. 5 for the comparison the ES+NC and ES+NC+CC measurements, and Fig. 6 for the comparison of the JUNO and JUNO + SNO flux

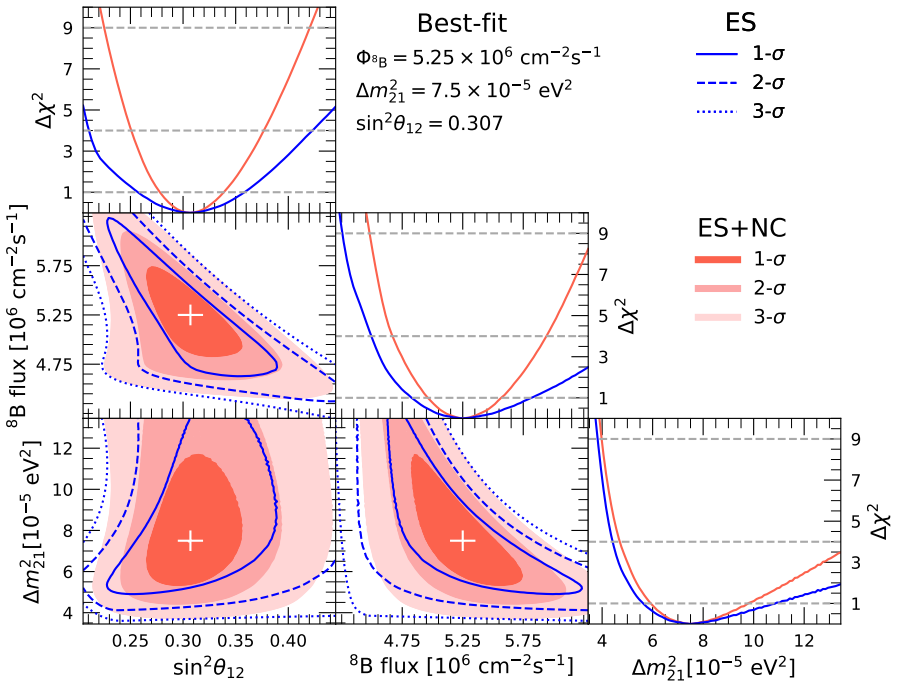

Figure 4: Comparison of the sensitivity on the ^{8}B solar neutrino flux, $\sin^2\theta_{12}$ and Δm^2_{21} between the ES measurement (single events outside [3.5, 4.1] MeV) and the ES+NC measurement (all singles events). The 1σ (68.3%), 2σ (95.5%), and 3σ (99.7%) allowed regions are illustrated with blue lines and red shaded regions, respectively. The marginalized projections of these parameters are also shown.

measurements. In addition, a summary of relative uncertainties on the ^{8}B neutrino flux, $\sin^2\theta_{12}$ and Δm^2_{21} from the model independent approach is provided in Fig. 7. Several important observations and comments are presented as follows.

- The NC measurement is accomplished based on the single events within [3.5, 4.1] MeV, where the background events are from the singles of ES and CC interactions of ^{8}B solar neutrinos, together with the natural radioactivity and muon-induced unstable isotopes. The standard MSW effect of solar neutrino oscillations is used in the calculation of ES and CC interactions and the oscillation parameters $\sin^2\theta_{12}$ and Δm^2_{21} are marginalized. The ^{8}B solar neutrino flux can be obtained with an accuracy of 10.6% with the NC measurement, which is comparable to the level of 8.6% from the NC measurement of the SNO Phase-III data [13].

- The ES measurement is based on the single events outside the energy range of [3.5, 4.1] MeV, in which the dominant background is from the natural radioactivity and muon-induced unstable isotopes, which are summarized in Fig. 2 and more details can be found in Ref. [27]. In the model independent approach of the ES measurement, the ^{8}B neutrino flux and two oscillation parameters $\sin^2\theta_{12}$ and Δm^2_{21} are simultaneously constrained, where the relative uncertainties are derived as $^{+11\%}_{-8\%}$, $^{+17\%}_{-17\%}$, and $^{+45\%}_{-25\%}$, respectively. The uncertainties of $\sin^2\theta_{12}$ and Δm^2_{21} are larger than those obtained in Ref. [27] by including the 3.8% SNO flux measurement because of the strong correlation between the flux and oscillation parameters in the model independent

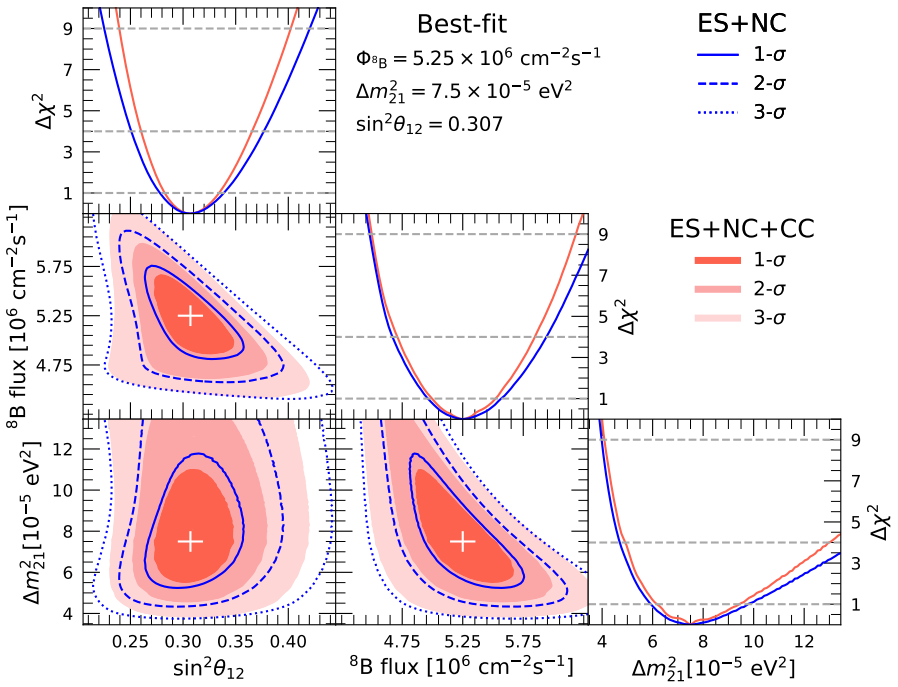

Figure 5: Same as Fig. 4, but for the comparison between the ES+NC measurement (all single events) and the ES+NC+CC measurement (both the single events and correlated events).

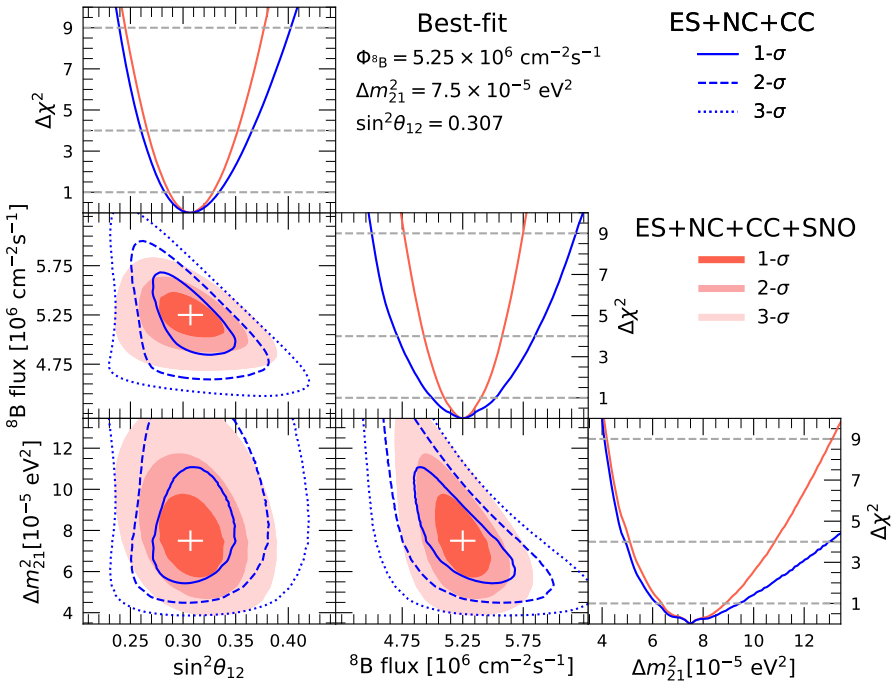

Figure 6: Same as Fig. 4, but for the comparison between the ES+NC+CC measurement of JUNO and the combined JUNO+SNO flux measurement.

approach. When adding the JUNO NC measurement, the accuracy of the ^{8}B neutrino flux can be improved to the level of $^{+6.0\%}_{-5.5\%}$, and the uncertainties of $\sin^2\theta_{12}$ and Δm^2_{21} are also improved to $^{+10\%}_{-10\%}$, and $^{+31\%}_{-21\%}$ respectively.

- The CC measurement with the correlated events itself cannot simultaneously determine the ^{8}B neutrino flux and oscillation parameters because of the high visible energy threshold. However, by combining the CC measurement with the single events of the NC+ES channels, it will help to break the correlation and possible degeneracy among different parameters, where the accuracy of the ^{8}B neutrino flux can be further improved to 5%, while those of $\sin^2\theta_{12}$ and Δm^2_{21} are $^{+9\%}_{-8\%}$, and $^{+25\%}_{-17\%}$ respectively.

- The expected 5% precision of the ^{8}B neutrino flux obtained with all three detection channels is much better than that of 11.6% from the latest prediction of the SSM [24]. This will be the only model independent measurement after SNO [14]. In addition, the uncertainties of $\sin^2\theta_{12}$ and Δm^2_{21} from the ^{8}B neutrino measurement at JUNO are at the levels of $^{+9\%}_{-8\%}$ and $^{+25\%}_{-17\%}$ respectively, which is comparable to the levels of $^{+5\%}_{-5\%}$, and $^{+20\%}_{-11\%}$ from the latest results of combined SK and SNO solar neutrino data [49]. Considering that the reactor antineutrino measurement of JUNO will obtain sub-percent levels of $\sin^2\theta_{12}$ and Δm^2_{21} in the near future [50], measurements of these parameters from future solar neutrino data would be important to test the CPT symmetry of fundamental physics and resolve the possible discrepancy between the neutrino and antineutrino oscillation channels.

- Within the spirit of the model independent approach, one can also include the 3.8% ^{8}B neutrino

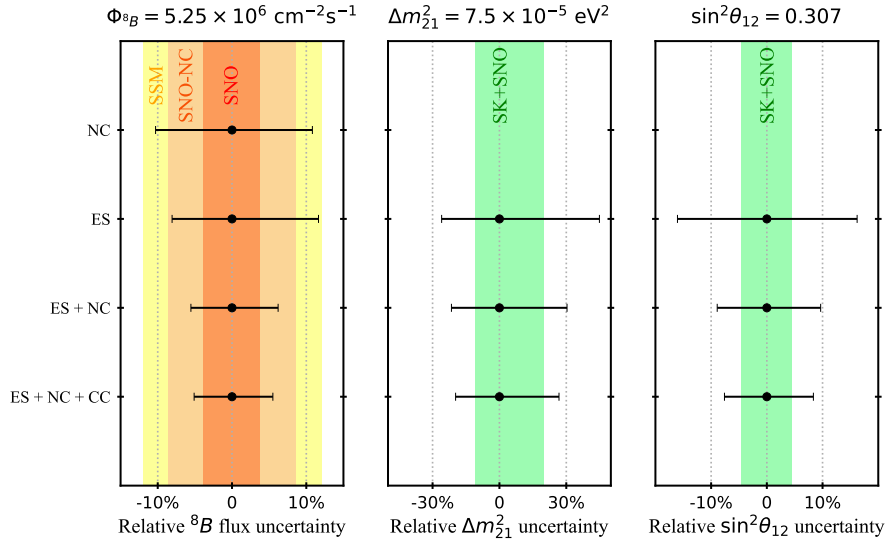

Figure 7: Relative uncertainties of the ^{8}B solar neutrino flux (left panel), Δm^2_{21} (middle panel), and $\sin^2\theta_{12}$ (right panel) from the model independent approach with different combinations of the data sets. The colored bands in the left panel are for the flux uncertainty from the SSM [24], the NC measurement of the SNO Phase-III data (SNO-NC) [13], and the combined SNO CC, NC and ES data (SNO) [14]. The green bands in the middle and right panels are the uncertainty of oscillation parameters from the combined SK and SNO solar neutrino data [49].

flux measurement of SNO as an informative prior, where even better precision levels of the flux and oscillation parameters can be achieved. In this scenario, the expected accuracy of the ^{8}B solar neutrino flux would reach the level of 3%, and $\sin^2\theta_{12}$ and Δm^2_{21} can be constrained with the precision of $^{+7.5\%}_{-6.5\%}$, and $^{+19\%}_{-15\%}$ respectively. These measurements are comparable to those from the current global solar neutrino data and would provide unique information to the future solar neutrino program.

- In addition to the discussion above, it is also noteworthy that the signal event rates and cross section uncertainties are the most crucial factors that affect the detection potential of the CC and NC detection channels. If the cross section uncertainties are 10%, instead of 1% assumed in this work, the uncertainty of the ^{8}B neutrino flux will become $^{+6\%}_{-6\%}$.

4 Concluding Remarks

In this work we have studied the physics potential of detecting ^{8}B solar neutrinos at JUNO, in a model independent manner by using the CC, NC and ES detection channels. Because of its largest-ever mass of ^{13}C and the expected low background level, excellent signal-to-background ratios can be achieved. Thus ^{8}B solar neutrinos will be observable in all three interaction channels.

We have performed detailed evaluations on the background budgets and signal efficiencies of the CC, NC and ES channels at JUNO. With optimized selection strategies, we find that the expected ^{8}B neutrino rates of the CC and NC channels are $\mathcal{O}(100)$ interactions per year after the event selection. It turns out that the signal event rates and cross section uncertainties are the most crucial factors that affect the detection potential of these two channels. We have carried out a combined analysis of both the coincidence and single events from all three detection channels, and shown that the ^{8}B

solar neutrino flux, $\sin^2\theta_{12}$, and Δm^2_{21} can be measured to $\pm5\%$, $^{+9\%}_{-8\%}$, and $^{+25\%}_{-17\%}$, respectively. When combined with the SNO flux measurement, the world-best precision of 3% can be achieved for the ^{8}B neutrino flux.

In the history of solar neutrino experiments, the NC measurement is unique in decoupling the neutrino flux and oscillation parameters, and enabling the model independent approach of the solar neutrino program. SNO has been the only solar neutrino experiment in the past to achieve this goal, and JUNO would be the second one. In this work, we have demonstrated the feasibility of ^{8}B solar neutrino measurements at JUNO, which, together with other large solar neutrino detectors [26,28,29], will open a new era of solar neutrino observation and may uncover new directions on neutrino physics and solar physics.

Acknowledgements

We are grateful for the ongoing cooperation from the China General Nuclear Power Group. This work was supported by the Chinese Academy of Sciences, the National Key R&D Program of China, the CAS Center for Excellence in Particle Physics, Wuyi University, and the Tsung-Dao Lee Institute of Shanghai Jiao Tong University in China, the Institut National de Physique Nucléaire et de Physique de Particules (IN2P3) in France, the Istituto Nazionale di Fisica Nucleare (INFN) in Italy, the Italian-Chinese collaborative research program MAECI-NSFC, the Fond de la Recherche Scientifique (F.R.S-FNRS) and FWO under the "Excellence of Science – EOS" in Belgium, the Conselho Nacional de Desenvolvimento Científico e Tecnològico in Brazil, the Agencia Nacional de Investigacion y Desarrollo and ANID - Millennium Science Initiative Program - ICN2019_044 in Chile, the Charles University Research Centre and the Ministry of Education, Youth, and Sports in Czech Republic, the Deutsche Forschungsgemeinschaft (DFG), the Helmholtz Association, and the Cluster of Excellence PRISMA+ in Germany, the Joint Institute of Nuclear Research (JINR) and Lomonosov Moscow State University in Russia, the joint Russian Science Foundation (RSF) and National Natural Science Foundation of China (NSFC) research program, the MOST and MOE in Taiwan, the Chulalongkorn University and Suranaree University of Technology in Thailand, University of California at Irvine and the National Science Foundation in USA.

Appendix

In this appendix, we present technical details of the sensitivity study used in this work. The Poisson-type least squares function χ^2 is defined as follows,

$$
\begin{aligned}
\chi^2 &= \chi^2_{\rm stat}({\rm CC}) + \chi^2_{\rm stat}({\rm NC}) + \chi^2_{\rm stat}({\rm ES}) + \chi^2_{\rm syst} \\
&= 2\times\sum_{i=1}^{10}\left[\sum_{j_{\rm C}=1}^{90}\left(N^{\rm C}_{\rm pre}(\theta^i_z,E^{j_{\rm C}}_{\rm vis}) - N^{\rm C}_{\rm obs}(\theta^i_z,E^{j_{\rm C}}_{\rm vis}) + N^{\rm C}_{\rm obs}(\theta^i_z,E^{j_{\rm C}}_{\rm vis})\cdot\log\frac{N^{\rm C}_{\rm obs}(\theta^i_z,E^{j_{\rm C}}_{\rm vis})}{N^{\rm C}_{\rm pre}(\theta^i_z,E^{j_{\rm C}}_{\rm vis})}\right)\right. \\
&+ \left.\sum_{j_{\rm S}=1}^{140}\left(N^{\rm S}_{\rm pre}(\theta^i_z,E^{j_{\rm S}}_{\rm vis}) - N^{\rm S}_{\rm obs}(\theta^i_z,E^{j_{\rm S}}_{\rm vis}) + N^{\rm S}_{\rm obs}(\theta^i_z,E^{j_{\rm S}}_{\rm vis})\cdot\log\frac{N^{\rm S}_{\rm obs}(\theta^i_z,E^{j_{\rm S}}_{\rm vis})}{N^{\rm S}_{\rm pre}(\theta^i_z,E^{j_{\rm S}}_{\rm vis})}\right)\right] \\
&+ \left(\frac{\varepsilon^{\rm ES}_X}{\sigma^{\rm ES}_X}\right)^2 + \left(\frac{\varepsilon^{\rm NC}_X}{\sigma^{\rm NC}_X}\right)^2 + \left(\frac{\varepsilon^{\rm CC}_X}{\sigma^{\rm CC}_X}\right)^2 + \sum_{k_{\rm C}}\left(\frac{\varepsilon^{k_{\rm C}}_{\rm B}}{\sigma^{k_{\rm C}}_{\rm B}}\right)^2 + \sum_{k_{\rm S}}\left(\frac{\varepsilon^{k_{\rm S}}_{\rm B}}{\sigma^{k_{\rm S}}_{\rm B}}\right)^2 \\
&+ \left(\frac{\varepsilon^{\rm C}_{\rm eff}}{\sigma^{\rm C}_{\rm eff}}\right)^2 + \left(\frac{\varepsilon^{\rm S}_{\rm eff}}{\sigma^{\rm S}_{\rm eff}}\right)^2 + (\varepsilon_{\rm s})^2 \,, \qquad (4)
\end{aligned}
$$

where $\chi^2_{\rm stat}$(CC), $\chi^2_{\rm stat}$(NC), and $\chi^2_{\rm stat}$(ES) are the statistical parts of the CC, NC and ES channels in the χ^2 function, respectively, which are shown in the second row and third row Eq. (4), with $j_{\rm C}$ from 1 to 90 for the CC measurement, $j_{\rm S}$ from 16 to 21 for the NC measurement, and $j_{\rm S}$ from 1 to 15 and from 22 to 140 for the ES measurement. $N^{\rm C}_{\rm pre}(\theta^i_z, E^{j_{\rm C}}_{\rm vis})$ and $N^{\rm S}_{\rm pre}(\theta^i_z, E^{j_{\rm S}}_{\rm vis})$ are the predicted numbers of the signal and background events in the i-th zenith angle bin, and the $j_{\rm C}$-th or $j_{\rm S}$-th visible energy bin of the correlated and single event samples, respectively, which can be calculated as

$$N^{\rm C}_{\rm pre}(\theta^i_z, E^{j_{\rm C}}_{\rm vis}) = (1+\varepsilon^{\rm C}_{\rm eff})S^{\rm CC}_{\rm pre}(\theta^i_z, E^{j_{\rm C}}_{\rm vis}) + \sum_{k_{\rm C}}(1+\varepsilon^{k_{\rm C}}_{\rm B})B^{k_{\rm C}}_{\rm pre}(\theta^i_z, E^{j_{\rm C}}_{\rm vis})\,, \quad (5)$$

$$N^{\rm S}_{\rm pre}(\theta^i_z, E^{j_{\rm S}}_{\rm vis}) = (1+\varepsilon^{\rm S}_{\rm eff})[S^{\rm NC}_{\rm pre}(\theta^i_z, E^{j_{\rm C}}_{\rm vis}) + S^{\rm ES}_{\rm pre}(\theta^i_z, E^{j_{\rm C}}_{\rm vis})] + \sum_{k_{\rm S}}(1+\varepsilon^{k_{\rm S}}_{\rm B})B^{k_{\rm S}}_{\rm pre}(\theta^i_z, E^{j_{\rm S}}_{\rm vis})\,, \quad (6)$$

where $S^{\rm CC}_{\rm pre}$, $S^{\rm NC}_{\rm pre}$, and $S^{\rm ES}_{\rm pre}$ are the two dimensional spectra of the ^{8}B neutrino signals in the CC, NC, and ES channels with the fiducial volume and signal efficiencies taken into account, whose projection in the axis of the visible energy can be found in Fig. 1 and Fig. 2 respectively. Meanwhile, $B^{k_{\rm C}}_{\rm pre}$ and $B^{k_{\rm S}}_{\rm pre}$ are components of the respective backgrounds in the correlated and single event samples, respectively, whose visible energy spectra are also illustrated in Fig. 1 and Fig. 2.

The calculations of the ^{8}B neutrino signal spectra in the CC, NC, and ES channels are given by

$$S^{\rm CC}_{\rm pre}(\theta^i_z, E^{j_{\rm C}}_{\rm vis}) = \Phi_{^8{\rm B}} \times \Big[(1+\varepsilon_{\rm s}\delta^{\rm S}_{E_\nu})S_{^8{\rm B}}(E_\nu) \otimes P_{ee}(\theta_{12}, \Delta m^2_{21}, E_\nu, \theta^i_z) \otimes (1+\varepsilon^{\rm CC}_X)\sigma_{\rm CC}(E_\nu, E_e) \otimes M(E_e, E^{j_{\rm C}}_{\rm vis})\Big]\,, \quad (7)$$

$$S^{\rm NC}_{\rm pre}(\theta^i_z, E^{j_{\rm C}}_{\rm vis}) = \Phi_{^8{\rm B}} \times \Big[(1+\varepsilon_{\rm s}\delta^{\rm S}_{E_\nu})S_{^8{\rm B}}(E_\nu) \otimes (1+\varepsilon^{\rm NC}_X)\sigma_{\rm NC}(E_\nu, E_\gamma) \otimes M(E_\gamma, E^{j_{\rm S}}_{\rm vis})\Big]\,, \quad (8)$$

$$S^{\rm ES}_{\rm pre}(\theta^i_z, E^{j_{\rm C}}_{\rm vis}) = \Phi_{^8{\rm B}} \times \Big\{(1+\varepsilon_{\rm s}\delta^{\rm S}_{E_\nu})S_{^8{\rm B}}(E_\nu) \otimes \Sigma_\alpha\Big[P_{e\alpha}(\theta_{12}, \Delta m^2_{21}, E_\nu, \theta^i_z) \otimes (1+\varepsilon^{\rm ES}_X)\sigma^{\nu_\alpha}_{\rm ES}(E_\nu, E_e)\Big] \otimes M(E_e, E^{j_{\rm C}}_{\rm vis})\Big\}\,, \quad (9)$$

which are the convolution of the ^{8}B neutrino spectrum $\Phi_{^8{\rm B}}$, the neutrino oscillation probability $P_{e\alpha}$ with $\alpha = e$ or $\mu+\tau$, the interaction cross section (i.e., $\sigma_{\rm CC}$, $\sigma_{\rm NC}$, and $\sigma^{\nu_\alpha}_{\rm ES}$) and the detector response matrix M. $P_{e\alpha}$ with both the standard MSW favor conversion and the terrestrial matter effect as the function of neutrino energy E_ν and the zenith angle θ_z is calculated in the three neutrino oscillation framework. The detector response matrix M includes the effects of both the energy resolution and energy non-linearity, which we directly follow the description in Ref. [27]. Finally, the observed spectra $N^{\rm C}_{\rm obs}(\theta^i_z, E^{j_{\rm C}}_{\rm vis})$ and $N^{\rm S}_{\rm obs}(\theta^i_z, E^{j_{\rm S}}_{\rm vis})$ can be obtained from the corresponding predicted spectra by taking the true values of the ^{8}B neutrino flux $\Phi_{^8{\rm B}}$ and oscillation parameters $\sin^2\theta_{12}$ and Δm^2_{21}, as well as the vanishing values of nuisance parameters. Note that, as discussed in Sec. 2, the ^{8}B solar neutrino interactions may also contribute to some of the background components $B^{k_{\rm C}}_{\rm pre}$ (e.g., the green line in Fig. 1, the purple line in Fig. 2), in this case, all possible correlation between the respective signal and background components will be taken into account in the χ^2 function.

The nuisance parameters ε^m_X (m=CC, NC, ES), $\varepsilon^k_{\rm B}$, $\varepsilon^n_{\rm eff}$ (n=C, S) correspond to the systematical uncertainties from the cross section, the backgrounds, and the detection efficiency that discussed in the manuscript. $\delta^{\rm S}_{E_\nu}$ is the 1σ fractional variation of the ^{8}B neutrino energy spectrum [30,31], and $\varepsilon_{\rm s}$

Table 3: Description the nuisance parameters and the associated uncertainties in the χ^2 function.

Sys.	Description for the pull term	Uncertainty
$\varepsilon_X^{\rm ES}$, $\varepsilon_X^{\rm NC}$, $\varepsilon_X^{\rm CC}$	Cross section for the CC, NC, ES channels	1%, 1%, 0.5%
$\varepsilon_{\rm eff}^{\rm C}$, $\varepsilon_{\rm eff}^{\rm S}$	Detector efficiency	2% [27]
$\varepsilon_{\rm B}^{k_{\rm C}}$, $\varepsilon_{\rm B}^{k_{\rm S}}$	Rate for the $k_{\rm C}$-th or $k_{\rm S}$-th background component	1%-10%, same as Ref. [27]
$\varepsilon_{\rm s}$	^{8}B neutrino energy spectrum	Refs. [30, 31]

denotes the magnitude of the ^{8}B neutrino spectral uncertainty. Description the nuisance parameters and the associated uncertainties in the χ^2 function is summarized in Table 3. In the sensitivity study of obtaining the results of Figs. 4-7, we first choose the data sets from one of the CC, NC and ES measurements or their combinations, and turn on the relevant nuisance parameters of the systematical uncertainties to formulate the respective χ^2 function. When the allowed regions of each analysis of are calculated, the displayed parameters (one or two of the fitting parameters $\Phi_{^8\rm B}$, θ_{12}, and Δm^2_{21}) will be fitted and all the other physical and nuisance will be marginalized. The critical values of $\Delta\chi^2$ for different confidence levels are taken from Ref. [17].

References

[1] R. Davis, Jr., D. S. Harmer, and K. C. Hoffman, Search for neutrinos from the sun, Phys. Rev. Lett. **20**, 1205 (1968).

[2] Kamiokande-II, K. S. Hirata et al., Observation of B-8 Solar Neutrinos in the Kamiokande-II Detector, Phys. Rev. Lett. **63**, 16 (1989).

[3] GALLEX, P. Anselmann et al., Solar neutrinos observed by GALLEX at Gran Sasso, Nucl. Phys. B Proc. Suppl. **31**, 117 (1993).

[4] GNO, M. Altmann et al., GNO solar neutrino observations: Results for GNO I, Phys. Lett. B **490**, 16 (2000).

[5] A. I. Abazov et al., Search for neutrinos from sun using the reaction Ga-71 (electron-neutrino e-) Ge-71, Phys. Rev. Lett. **67**, 3332 (1991).

[6] Super-Kamiokande, Y. Fukuda et al., Measurements of the solar neutrino flux from super-kamiokande's first 300 days, Phys. Rev. Lett. **81**, 1158 (1998).

[7] Super-Kamiokande, S. Fukuda et al., Solar b-8 and hep neutrino measurements from 1258 days of super-kamiokande data, Phys. Rev. Lett. **86**, 5651 (2001).

[8] H. H. Chen, Direct Approach to Resolve the Solar Neutrino Problem, Phys. Rev. Lett. **55**, 1534 (1985).

[9] SNO, Q. R. Ahmad et al., Measurement of the rate of $\nu_e + d \to p + p + e^-$ interactions produced by ^{8}b solar neutrinos at the sudbury neutrino observatory, Phys. Rev. Lett. **87**, 071301 (2001).

[10] SNO, Q. R. Ahmad et al., Direct evidence for neutrino flavor transformation from neutral-current interactions in the sudbury neutrino observatory, Phys. Rev. Lett. **89**, 011301 (2002).

[11] SNO, S. Ahmed et al., Measurement of the total active 8b solar neutrino flux at the sudbury neutrino observatory with enhanced neutral current sensitivity, Phys. Rev. Lett. **92**, 181301 (2004).

[12] SNO, B. Aharmim et al., An independent measurement of the total active 8b solar neutrino flux using an array of 3he proportional counters at the sudbury neutrino observatory, Phys. Rev. Lett. **101**, 111301 (2008).

[13] SNO, B. Aharmim et al., Measurement of the ν_e and Total ^{8}B Solar Neutrino Fluxes with the Sudbury Neutrino Observatory Phase-III Data Set, Phys. Rev. C **87**, 015502 (2013).

[14] SNO, B. Aharmim et al., Combined Analysis of all Three Phases of Solar Neutrino Data from the Sudbury Neutrino Observatory, Phys. Rev. C **88**, 025501 (2013).

[15] L. Wolfenstein, Neutrino oscillations in matter, Phys. Rev. **D17**, 2369 (1978).

[16] S. P. Mikheev and A. Y. Smirnov, Resonance enhancement of oscillations in matter and solar neutrino spectroscopy, Sov. J. Nucl. Phys. **42**, 913 (1985).

[17] Particle Data Group, P. A. Zyla et al., Review of Particle Physics, PTEP **2020**, 083C01 (2020).

[18] Super-Kamiokande, K. Abe et al., Solar Neutrino Measurements in Super-Kamiokande-IV, Phys. Rev. D **94**, 052010 (2016).

[19] Super-Kamiokande, A. Renshaw et al., First Indication of Terrestrial Matter Effects on Solar Neutrino Oscillation, Phys. Rev. Lett. **112**, 091805 (2014).

[20] BOREXINO, G. Bellini et al., Neutrinos from the primary proton–proton fusion process in the Sun, Nature **512**, 383 (2014).

[21] BOREXINO, M. Agostini et al., Experimental evidence of neutrinos produced in the CNO fusion cycle in the Sun, Nature **587**, 577 (2020).

[22] J. Arafune, M. Fukugita, Y. Kohyama, and K. Kubodera, C-13 AS A SOLAR NEUTRINO DETECTOR, Phys. Lett. B **217**, 186 (1989).

[23] A. Ianni, D. Montanino, and F. L. Villante, How to observe B-8 solar neutrinos in liquid scintillator detectors, Phys. Lett. B **627**, 38 (2005).

[24] N. Vinyoles et al., A new Generation of Standard Solar Models, Astrophys. J. **835**, 202 (2017).

[25] I. Esteban, M. C. Gonzalez-Garcia, M. Maltoni, T. Schwetz, and A. Zhou, The fate of hints: updated global analysis of three-flavor neutrino oscillations, JHEP **09**, 178 (2020).

[26] F. Capozzi, S. W. Li, G. Zhu, and J. F. Beacom, DUNE as the Next-Generation Solar Neutrino Experiment, Phys. Rev. Lett. **123**, 131803 (2019).

[27] JUNO, A. Abusleme et al., Feasibility and physics potential of detecting ^{8}B solar neutrinos at JUNO, Chin. Phys. C **45**, 023004 (2021).

[28] Hyper-Kamiokande, K. Abe et al., Hyper-Kamiokande Design Report, (2018), arXiv:1805.04163.

[29] Jinping, J. F. Beacom et al., Physics prospects of the Jinping neutrino experiment, Chin. Phys. C **41**, 023002 (2017).

[30] J. N. Bahcall et al., Standard neutrino spectrum from B-8 decay, Phys. Rev. C **54**, 411 (1996).

[31] J. N. Bahcall, Gallium solar neutrino experiments: Absorption cross-sections, neutrino spectra, and predicted event rates, Phys. Rev. C **56**, 3391 (1997).

[32] M. Fukugita, Y. Kohyama, and K. Kubodera, NEUTRINO REACTION CROSS-SECTIONS ON C-12 TARGET, Phys. Lett. B **212**, 139 (1988).

[33] T. Suzuki, A. B. Balantekin, and T. Kajino, Neutrino Capture on ^{13}C, Phys. Rev. C **86**, 015502 (2012).

[34] T. Suzuki, A. B. Balantekin, T. Kajino, and S. Chiba, Neutrino-13C Cross Sections at Supernova Neutrino Energies, J. Phys. G **46**, 075103 (2019).

[35] JUNO, T. Lin et al., The Application of SNiPER to the JUNO Simulation, J. Phys. Conf. Ser. **898**, 042029 (2017).

[36] J. H. Zou et al., SNiPER: an offline software framework for non-collider physics experiments, J. Phys. Conf. Ser. **664**, 072053 (2015).

[37] E. D. Carlson, Terrestrially Enhanced Neutrino Oscillations, Phys. Rev. D **34**, 1454 (1986).

[38] A. J. Baltz and J. Weneser, Effect of transmission through the earth on neutrino oscillations, Phys. Rev. **D35**, 528 (1987).

[39] A. J. Baltz and J. Weneser, Matter oscillations: neutrino transformation in the sun and regeneration in the earth, Phys. Rev. **D37**, 3364 (1988).

[40] P. I. Krastev and S. T. Petcov, Resonance Amplification and t Violation Effects in Three Neutrino Oscillations in the Earth, Phys. Lett. B **205**, 84 (1988).

[41] M. Blennow, T. Ohlsson, and H. Snellman, Day-night effect in solar neutrino oscillations with three flavors, Phys. Rev. D **69**, 073006 (2004).

[42] E. K. Akhmedov, M. A. Tortola, and J. W. F. Valle, A Simple analytic three flavor description of the day night effect in the solar neutrino flux, JHEP **05**, 057 (2004).

[43] P. C. de Holanda, W. Liao, and A. Y. Smirnov, Toward precision measurements in solar neutrinos, Nucl. Phys. B **702**, 307 (2004).

[44] W. Liao, Precise Formulation of Neutrino Oscillation in the Earth, Phys. Rev. D **77**, 053002 (2008).

[45] H. W. Long, Y. F. Li, and C. Giunti, Day-Night Asymmetries in Active-Sterile Solar Neutrino Oscillations, JHEP **08**, 056 (2013).

[46] JUNO, A. Abusleme et al., JUNO physics and detector, Prog. Part. Nucl. Phys. **123**, 103927 (2022), arXiv:2104.02565.

[47] B. R. Barrett, P. Navratil, and J. P. Vary, Ab initio no core shell model, Prog. Part. Nucl. Phys. **69**, 131 (2013).

[48] O. Tomalak and R. J. Hill, Theory of elastic neutrino-electron scattering, Phys. Rev. D **101**, 033006 (2020).

[49] Y. Nakajima, Recent results and future prospects from Super- Kamiokande, talk at Neutrino 2020.

[50] JUNO, A. Abusleme et al., Sub-percent Precision Measurement of Neutrino Oscillation Parameters with JUNO, arXiv:2204.13249.